



HAL
open science

Multiwavelength observations of the binary system PSR B1259-63/LS 2883 around the 2010-2011 periastron passage

M. Chernyakova, A.A. Abdo, A. Neronov, M.V. Mcswain, J. Moldón, M. Ribó, J.M. Paredes, I. Sushch, M. de Naurois, U. Schwanke, et al.

► To cite this version:

M. Chernyakova, A.A. Abdo, A. Neronov, M.V. Mcswain, J. Moldón, et al.. Multiwavelength observations of the binary system PSR B1259-63/LS 2883 around the 2010-2011 periastron passage. Monthly Notices of the Royal Astronomical Society, 2014, 439 (1), pp.432-445. 10.1093/mnras/stu021 . hal-01087272

HAL Id: hal-01087272

<https://hal.science/hal-01087272>

Submitted on 7 Jan 2022

HAL is a multi-disciplinary open access archive for the deposit and dissemination of scientific research documents, whether they are published or not. The documents may come from teaching and research institutions in France or abroad, or from public or private research centers.

L'archive ouverte pluridisciplinaire **HAL**, est destinée au dépôt et à la diffusion de documents scientifiques de niveau recherche, publiés ou non, émanant des établissements d'enseignement et de recherche français ou étrangers, des laboratoires publics ou privés.



Distributed under a Creative Commons Attribution 4.0 International License

Multiwavelength observations of the binary system PSR B1259–63/LS 2883 around the 2010–2011 periastron passage

M. Chernyakova,^{1,2★} A. A. Abdo,³ A. Neronov,⁴ M. V. McSwain,⁵ J. Moldón,^{6,7}
M. Ribó,⁶ J. M. Paredes,⁶ I. Sushch,^{8,9,10} M. de Naurois,¹¹ U. Schwanke,¹⁰
Y. Uchiyama,^{12,13} K. Wood,¹⁴ S. Johnston,¹⁵ S. Chaty,^{16,17} A. Coleiro,¹⁶
D. Malyshev^{4,18} and Iu. Babyk^{1,2}

¹Dublin City University, Dublin 9, Ireland

²Dublin Institute for advanced studies, 31 Fitzwilliam Place, Dublin 2, Ireland

³Operational Evaluation Division, Institute for Defense Analyses, 4850 Mark Center Drive Alexandria, VA 22311-1882, USA

⁴INTEGRAL Science Data Center, Chemin d'Écogia 16, CH-1290 Versoix, Switzerland

⁵Department of Physics, Lehigh University, 16 Memorial Drive East, Bethlehem, PA 18015, USA

⁶Departament d'Astronomia i Meteorologia, Institut de Ciències del Cosmos, Universitat de Barcelona, IEEC-UB, Martí i Franquès 1, E-08028 Barcelona, Spain

⁷The Netherlands Institute for Radio Astronomy (ASTRON), NL-7990-AA Dwingeloo, the Netherlands

⁸Centre for Space Research, North-West University, Potchefstroom Campus, 2520 Potchefstroom, South Africa

⁹Astronomical Observatory of Ivan Franko National University of L'viv, vul. Kyryla i Methodia, 8, L'viv 79005, Ukraine

¹⁰Institut für Physik, Humboldt-Universität zu Berlin, Newtonstr. 15, D-12489 Berlin, Germany

¹¹Laboratoire Leprince-Ringuet, Ecole Polytechnique, CNRS/IN2P3, F-91128 Palaiseau, France

¹²SLAC National Accelerator Laborat 2575 Sand Hill Road, Menlo Park, CA 94025, USA

¹³Department of Physics, Rikkyo University, Nishi-Ikebukuro 3-34-1, Toshima-ku, Tokyo 171-8501, Japan

¹⁴U.S. Naval Research Lab 4555 Overlook Ave., SW Washington, DC 20375, USA

¹⁵CSIRO Astronomy and Space Science, PO BOX 76, NSW 1710, Australia

¹⁶Laboratoire AIM (UMR-E 9005 CEA/DSM – CNRS – Université Paris Diderot), Irfu / Service d'Astrophysique, CEA-Saclay, F-91191 Gif-sur-Yvette Cedex, France

¹⁷Institut Universitaire de France, 103 Boulevard Saint Michel, F-75006 Paris, France

¹⁸Bogolyubov Institute for Theoretical Physics, 14-b Metrolohichna street, Kiev 03680, Ukraine

Accepted 2013 December 19. Received 2013 December 19; in original form 2013 September 23

ABSTRACT

We report on broad multiwavelength observations of the 2010–2011 periastron passage of the γ -ray loud binary system PSR B1259–63. High-resolution interferometric radio observations establish extended radio emission trailing the position of the pulsar. Observations with the *Fermi Gamma-ray Space Telescope* reveal GeV γ -ray flaring activity of the system, reaching the spin-down luminosity of the pulsar, around 30 d after periastron. There are no clear signatures of variability at radio, X-ray and TeV energies at the time of the GeV flare. Variability around periastron in the H α emission line, can be interpreted as the gravitational interaction between the pulsar and the circumstellar disc. The equivalent width of the H α grows from a few days before periastron until a few days later, and decreases again between 18 and 46 d after periastron. In near-infrared we observe the similar decrease of the equivalent width of Br γ line between the 40th and 117th day after the periastron. For the idealized disc, the variability of the H α line represents the variability of the mass and size of the disc. We discuss possible physical relations between the state of the disc and GeV emission under assumption that GeV flare is directly related to the decrease of the disc size.

Key words: stars: emission-line, Be – pulsars: individual: PSR B1259–63 – gamma-rays: stars – X-rays: binaries – X-rays: individual: PSR B1259–63.

1 INTRODUCTION

The binary system PSR B1259–63 is comprised of a 47.76 ms radio pulsar in a highly eccentric orbit ($e \approx 0.87$, $P \approx 3.4$ yr) around the massive main sequence O9.5Ve star LS 2883 (Johnston et al. 1992;

* E-mail: masha.chernyakova@dcu.ie

Negueruela et al. 2011). The companion shows evidence for an equatorial disc in its optical spectrum, and it has generally been classified as a Be star. The minimum approach between the pulsar and massive star is about ~ 0.9 au (Negueruela et al. 2011), which is roughly the size of the equatorial disc (Johnston et al. 1992). The orbital plane of the pulsar is thought to be inclined with respect to this disc, so it crosses the disc plane twice each orbit, just before and just after the periastron passage (e.g. Melatos, Johnston & Melrose 1995). A shock interaction between the relativistic pulsar wind and the wind and photon field of the Be star is believed to give rise to the observed unpulsed X-ray emission observed throughout the orbit (Hirayama et al. 1999; Chernyakova et al. 2006) and the unpulsed radio and TeV γ -rays observed within a few months of periastron passage (Johnston et al. 1999, 2005; Kirk, Ball & Skjaeraasen 1999; Aharonian et al. 2005, 2009).

The emission from the system varies dramatically as the pulsar moves through very different environments, making it an excellent test bed for models of a shocked pulsar wind. When the pulsar is far from periastron, the highly linearly polarized pulsed radio emission is detected (Johnston et al. 1999, 2005). As the pulsar approaches the companion star ($\sim t_p - 100$ d, where t_p is the time of periastron passage), depolarization of the pulsed emission occurs, and the dispersion measure (DM) and absolute value of the rotation measure (RM) begin to increase while the pulsed flux density decreases (Johnston et al. 1996). In the range $\sim t_p \pm 15$ d, no pulsed flux is detected (Johnston et al. 1996). The eclipse of the pulsar during this period is likely due to absorption and severe pulse scattering by the Be star’s disc (Johnston et al. 1996). This eclipse of the pulsed emission is accompanied by an increase in the unpulsed radio flux beginning at $\sim t_p - 30$ d and reaching a maximum at about $t_p - 10$ d. It then decreases around the periastron passage before climbing to a second peak about 20 d after the periastron passage (Johnston et al. 1999, 2005), finally declining over $\sim t_p + 100$ d. Unpulsed flux at the two peaks before and after periastron passage can be several times higher than the value during the periastron passage.

The radio emission has been imaged at scales of au with the Australian Long Baseline Array (LBA), revealing that it extends up to projected distances of more than 100 au close to the periastron passage (Moldón et al. 2011). The peak of this radio emission is detected at projected distances of several tens of au outside the binary system (provided unmodelled ionospheric uncertainties are not very large). This has been the first observational evidence that non-accreting pulsars orbiting massive stars can produce variable extended radio emission at au scales. It must be noted that similar structures have been detected in the γ -ray binaries LS 5039 and LS I +61 303, reinforcing the links between these three sources and supporting the presence of pulsars in these systems as well (Moldón, Ribó & Paredes 2012 and references therein).

In the X-ray band, variable unpulsed emission is observed throughout the orbit (Chernyakova et al. 2009, and references therein), even at apastron. For most of the orbit, the typical X-ray flux is of the order of $F_X \sim 10^{-12}$ erg cm $^{-2}$ s $^{-1}$. Commencing 20–30 d prior to periastron passage, there is a sharp rise, reaching 10–20 times the apastron flux. After that, the flux decreases by a factor of a few to a local minimum near or after periastron passage, then to a post-periastron second maximum similar to the pre-periastron maximum, following which it declines over 100–150 d. This twofold X-ray maximum broadly resembles the unpulsed radio light curve. Moreover, the X-ray pattern is essentially repeated during each orbit, without large orbit-to-orbit variations.

Apart from the variable X-ray emission from the binary system itself, Pavlov, Chang & Kargaltsev (2011) have recently reported

the discovery of extended X-ray emission on distance scales much larger than the size of the binary orbit (4 arcsec, corresponding to a projected distance of $\sim 10^{17}$ cm). This indicates that the pulsar is also powering a ‘regular’ pulsar wind nebula during the periods outside the periastron passage.

At energies around 1 GeV, the *Energetic Gamma-Ray Experiment Telescope* produced only an upper limit for the 1994 periastron passage ($F_\gamma \leq 9.4 \times 10^{-8}$ photons cm $^{-2}$ s $^{-1}$ for $E \geq 300$ MeV, 95 per cent confidence; Tavani et al. 1996), and there was no opportunity to observe at these energies during the next four periastron passages. However, in TeV γ -rays the system was detected during the 2004 and 2007 periastron passages (Aharonian et al. 2005, 2009), and flux variations on daily time-scales from zero to 10^{-11} cm $^{-2}$ s $^{-1}$ were seen for energies > 0.38 TeV in 2004 (Aharonian et al. 2005). A combined light curve of those two periastron passages reveals a hint of two asymmetrical peaks centred around periastron with a decrease of the flux at the periastron itself. Peaks of the TeV emission roughly coincide with the flux enhancement observed in other wavebands as well as the eclipse of the pulsed radio emission. In 2007, the photon flux became notable at the level of 3 standard deviations (σ) from $\sim t_p - 75$ d onwards. No TeV detection has been reported far from periastron (Aharonian et al. 2009).

The most recent periastron passage took place on 2010 December 14, 16:40:50.6 (MJD 555 44.7). For the first time, we had a chance to observe it in GeV range with the Large Area Telescope (LAT) of *Fermi* satellite. No detection at the level of 5σ was observed from the source on daily and weekly time-scales prior to 28 d before the periastron, $t_p - 28$ d. Integrating from $t_p - 28$ d (the typical start of enhanced X-ray and unpulsed radio flux) to periastron yielded a clear detection of excess gamma-ray flux from the source at a 5σ level in the energy range 0.1–1 GeV. The source disappeared after $t_p + 18$ d and suddenly became bright again 30 days after the periastron, reaching a flux ~ 10 times higher than the integrated flux measured during the periastron passage (Abdo et al. 2011b; Tam et al. 2011). This flare lasted for about seven weeks with no corresponding rise in X-ray or radio domains (Abdo et al. 2011b).

Here we report on the multiwavelength observations of PSR B1259–63 over ~ 20 decades of energy, from radio to TeV γ -rays, during its 2010 periastron passage. The paper is organized in the following way: in Section 2 we describe radio observations, in Section 3 we report NIR observations, in Section 4 we discuss optical observations, Sections 5, 6 and 7 are devoted to X-ray, GeV and TeV observations, respectively. The discussion of all the results is in Section 8, and finally the conclusions are in Section 9.

2 RADIO OBSERVATIONS AND RESULTS

2.1 Pulse monitoring with Parkes

PSR B1259–63 is one of the pulsars regularly timed with the Parkes radio telescope as part of the *Fermi* timing consortium (Smith et al. 2008; Weltevrede et al. 2010). In order to look for changes in the DM and RM and to determine the duration of the eclipse of the pulsed signal, we monitored the pulsar with Parkes during the 2010 periastron passage. The last detection of pulsed emission in 2010 happened 18 d before the periastron ($t = t_p - 18$ d). The first observation with no pulsations happened at $t_p - 16$ d. Significant changes in the DM were observed during ~ 2 weeks leading to the disappearance of the pulse. Pulsation was re-detected on $t_p + 15$ d at 3.1 GHz and subsequently at lower frequencies ($t_p + 16$ d at 1.4 GHz). The moments when the pulsed emission disappears (last

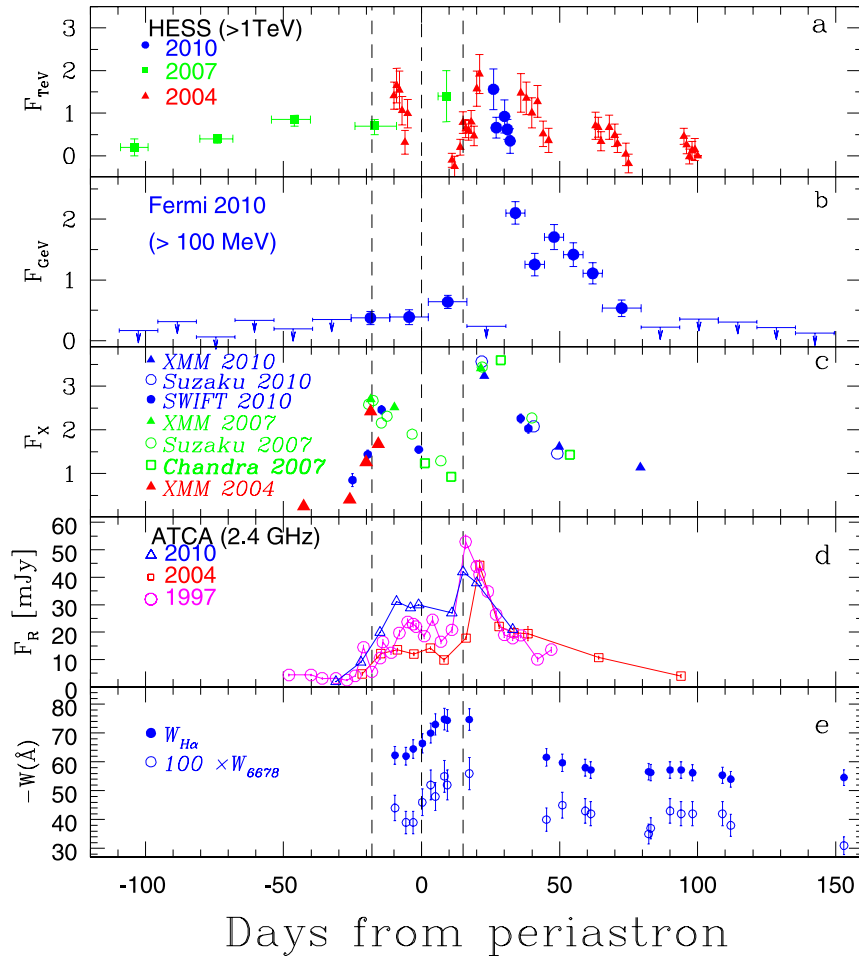


Figure 1. Orbital light curves of PSR B1259–63 around periastron for several passages. Panel a: observations by HESS in the $E > 1$ TeV energy range for the 2004, 2007 and 2010 periastron passages (Aharonian et al. 2005, 2009; HESS Collaboration 2013). Flux is given in $10^{-12} \text{ cm}^{-2} \text{ s}^{-1}$. Panel b: *Fermi*-LAT flux measurements in the $E > 100$ MeV energy range for the 2010 periastron passage. Flux is given in $10^{-6} \text{ cm}^{-2} \text{ s}^{-1}$. Panel c: X-ray fluxes from three periastron passages (Chernyakova et al. 2009; Abdo et al. 2011b). Flux is given in $10^{-11} \text{ erg cm}^{-2} \text{ s}^{-1}$. The typical error of the X-ray data is smaller than the size of the symbols. Panel d: radio (2.4 GHz) flux densities measured at ATCA for the 2010, 2004 and 1997 periastron passages (Johnston et al. 2005, 1999; Abdo et al. 2011b). Dashed lines correspond to the periastron and to the moments of disappearance (last detection) and reappearance (first detection) of the pulsed emission. Panel e: evolution of the EWs of $H\alpha$ (filled circles) and $\text{He I } \lambda 6678$ (open circles). W_{6678} is shown multiplied by a factor of 100 for easier comparison to $W_{H\alpha}$.

detection) and reappears (first detection) are marked with dashed lines in Fig. 1.

2.2 ATCA observations

Monitoring of the unpulsed radio signal was performed with the Australia Telescope Compact Array (ATCA). We monitored PSR B1259–63 at frequencies between 1.1 and 10 GHz. A total of 12 observations were collected in the period between $t_p - 31$ and $t_p + 55$ d. Unpulsed radio emission was detected throughout the periastron passage with a behaviour similar to that seen in previous periastron passages (Johnston et al. 2005; Abdo et al. 2011b). Panel d of Fig. 1 shows the radio light curve for the 1997, 2004 and 2010 periastron passages.

2.3 LBA observations of PSR B1259–63

2.3.1 LBA observations and data reduction

Very long baseline interferometer (VLBI) observations of PSR B1259–63 were conducted with the Australian LBA at

2.3 GHz (13 cm) on 2011 January 13 (MJD 55574), from 12:00 to 23:55 UTC. The orbital phase of the binary system during the observation was 0.243, computed using the ephemerides in Wang, Johnston & Manchester (2004) and corresponds to 29.3 d after the periastron passage. Six antennas participated in the observations: ATCA (as a phased array), Ceduna, Hobart, Mopra, Parkes and Tidbinbilla (we note that the data from Tidbinbilla could not be properly calibrated and were not included in the final data reduction).

The data were obtained with dual circular polarization. ATCA, Mopra and Parkes recorded eight 16 MHz subbands (four for each right- and left-handed polarization) for a total data bit rate of 512 Mbps per station, and the rest of the antennas recorded four 16 MHz subbands, for a total bit rate of 256 Mbps. The correlation of the data was conducted at the correlator in the International Centre for Radio Astronomy Research, which produced the final visibilities with an integration time of 2 s. Two passes of the correlator were conducted: one with all the data and for all sources, and a second one correlated only during the on-pulse of PSR B1259–63 using pulsar binning. The pulsar ephemerides were obtained from long-term timing observations conducted with Parkes.

The observations were performed using phase referencing on the calibrator J1256–6449, located at $1^{\circ}2'$ from PSR B1259–63. J1256–6449 was correlated at $\alpha_{J2000.0} = 12^{\text{h}}56^{\text{m}}03^{\text{s}}.4032$ and $\delta_{J2000.0} = -64^{\circ}49'14''.814$, which has an absolute uncertainty in the International Celestial Reference Frame (ICRF) of 2.8 mas in right ascension and in declination. The cycle time was 6 min, spending half of the time on the phase calibrator and the target source alternatively. The sources J1332–6646 and J1352–4412 were observed as fringe finders.

The data reduction was performed using the National Radio Astronomy Observatory Astronomical Image Processing System (AIPS).¹ We applied a priori flagging on telescope off-source times because of antenna slewing, and ionospheric corrections obtained from total electron content models based on GPS data obtained from the Crustal Dynamics Data Information System (CDDIS) data archive.² The amplitude calibration was performed using the system temperatures measured at each station, although no antenna gain curves were available. The amplitude calibration was fixed by scaling the individual antenna gains by a factor obtained from the phase calibrator and fringe-finder models. This correction scales the visibility amplitudes between antennas, and therefore the measured source flux density is not reliable. The phase calibration was obtained from the phase reference calibrator J1256–6449 using the AIPS task FRING. The phase solutions were applied to the data of PSR B1259–63. We produced an image of PSR B1259–63 using the task IMAGR, with robust parameter 0, and uv tapering of $8 M\lambda$ to reduce the weight of the longest and more noisy baselines. We further calibrated the data with several iteration steps of phase only and phase+amplitude self-calibrations. Due to the limited number of antennas, for amplitude self-calibration we always used integration time intervals of at least 6 h (half of the total 12-h observation time). The integration time of the phase self-calibration steps was 10 min, and this was reduced to 2 and 1 min in the last steps.

The amplitude and phase calibration tables from the phase reference source were also applied to the on-pulse data of PSR B1259–63. In this data set the flux density of the pulsed emission is slightly enhanced, whereas for the unpulsed emission, i.e. extended nebula, it remains equal. We produced self-calibrated images following the same procedure described above. We subtracted the image obtained using the whole data from the image obtained using the on-pulse data only, taking into account a scaling factor for the amplitudes. The resulting image shows a point-like source at the position of the enhanced pulsed emission and therefore marks the position of the pulsar.

2.3.2 LBA results

The phase-referenced data provide an accurate determination of the position of PSR B1259–63 with respect to the phase calibrator. The measured position of the peak of the source in the ICRF is $\alpha_{J2000.0} = 13^{\text{h}}02^{\text{m}}47^{\text{s}}.64239 \pm 0.3 \text{ mas}$ ($\pm 2.8 \text{ mas}$) and $\delta_{J2000.0} = -63^{\circ}50'08''.6267 \pm 0.3 \text{ mas}$ ($\pm 2.8 \text{ mas}$), where the first set of uncertainties correspond to the formal errors of a Gaussian fit obtained with JMFIT within AIPS, and the uncertainties in parenthesis correspond to the absolute uncertainty of the phase calibrator position in the ICRF. Additional systematic errors due to the unmodelled ionosphere of 1–5 mas are expected. We note that the source is intrinsically extended (see Moldón et al. 2011) and therefore the

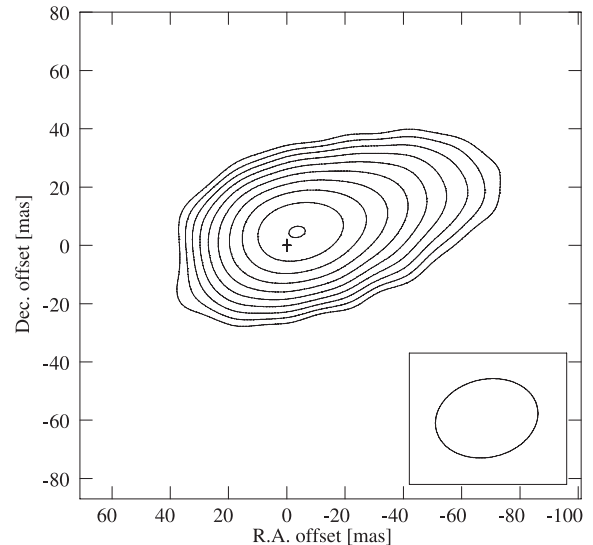


Figure 2. Self-calibrated LBA image of PSR B1259–63 obtained on 2011 January 13 (29 d after periastron passage) at 2.3 GHz frequency. The contours start at three times the rms of the image and increase by factors of $2^{1/2}$, up to a peak S/N of 68. The (0,0) coordinates correspond to the position of the pulsar. The cross represents the pulsar position uncertainty at the 5σ level. The synthesized beam, plotted in the lower-right corner, has a size of $35.5 \times 26.7 \text{ mas}^2$ and is oriented with PA of -77° .

astrometry depends on the resolution of the observation, which for the phase-referenced image is $18.4 \times 14.6 \text{ mas}^2$ at 87° .

In Fig. 2 we show the final self-calibrated image of PSR B1259–63 obtained 29 d after the periastron passage. The structure is similar to the one reported in Moldón et al. (2011) 21 d after the previous periastron passage. The source shows a main core and extended diffuse emission towards the north-west. In this image, for the first time, we have an accurate position of the pulsar within the unpulsed extended nebula.

The extended emission has a total size of $\sim 50 \text{ mas}$ with a position angle (PA) of approximately -75° . Visual inspection of higher resolution images shows that the structure is dominated by a bright compact core and a diffuse component. We fitted two components to the interferometric uv plane using the task UVFIT. We found that the core is well fitted by a point-like component, whereas the diffuse emission is described by a circular Gaussian component with a full width at half-maximum (FWHM) of 20 mas located at -32.0 ± 0.2 and $8.7 \pm 0.2 \text{ mas}$ from the core in right ascension and declination, respectively. It was not possible to fit an additional component for the pulsar, which is too faint to be distinguished from the core component with the current noise level.

The position of the pulsar, obtained from the difference between the gated and the ungated data, is $3.1 \pm 0.3 \text{ mas}$ in right ascension and $-4.6 \pm 0.4 \text{ mas}$ in declination from the core component as seen with the current resolution, for a total separation of $5.6 \pm 0.4 \text{ mas}$. The position of the pulsar is marked with a cross in Fig. 2, and its size is the estimated uncertainty at 5σ level. The uncertainty in the relative astrometry of the pulsar comes from the limitation of efficiently subtracting the nebula contribution in the two images (gated and ungated), mainly because of small differences in the self-calibration and the determination of the scaling factor for the amplitudes, which is 0.25. We explored a range of the scaling factors between 0.15 and 0.35 and considered only those images showing a point-like source, i.e. for which the nebula was completely subtracted. We measured the pulsar position in each image,

¹ AIPS is available online at <http://www.aips.nrao.edu/>

² CDDIS is available online at <http://cddis.nasa.gov/>

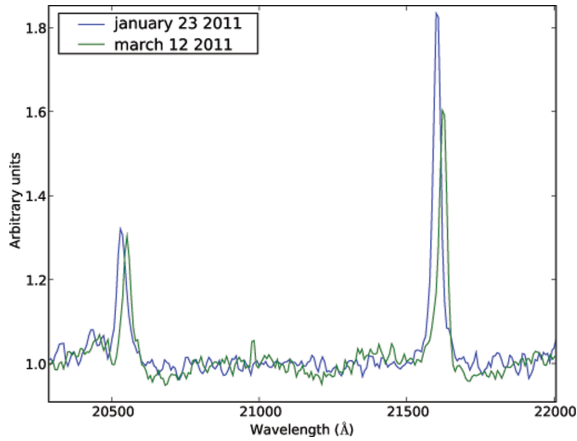


Figure 3. ESO/VLT NIR K_s -band spectra obtained on 2011 January 23 and March 12.

which followed a linear displacement as a function of the scaling factor. The maximum separation of these peak positions was divided by 2 to estimate the position uncertainty. An independent estimate of the position uncertainty comes from the fitting procedure of the JMFIT task within AIPS. We have considered the higher of these two values in each coordinate as the estimate of the 1σ uncertainty in position, which turns out to be 0.3 mas in right ascension and 0.4 mas in declination. The cross plotted in Fig. 2 represents five times these values to be on the conservative side, given possible differences related to the self-calibration processes.

3 INFRARED SPECTROSCOPY

We performed European Southern Observatory (ESO) Very Large Telescope (VLT) observations of PSR B1259–63 on Unit Telescope 1 (UT1-Antu), using the Target of Opportunity (ToO) programme ID 086.D-0511 (PI Chaty) dedicated to optical/infrared study of high-energy transients in support to *Fermi* observations. We obtained low-resolution ($R \sim 750$) infrared spectra with the Infrared Spectrometer And Array Camera (ISAAC) instrument in near-infrared (NIR, SWS-LR JHK_s 1–2 μm) on 2011 January 22/23 and March 12. The ToO was activated on two dates spaced by ~ 1.5 month, 2011 in January and March, to compare two different sets of data, and potentially detect spectral variability of the source. Because of the brightness of the NIR counterpart ($K_s = 7.248$), and to avoid non-linearity, the exposure time of individual ISAAC SW spectra was set to 3.55 s. Observations were carried out under clear conditions with a seeing ranging from 0.35 to 0.50 arcsec. Spectra analysis was standard, including zero correction, flat-field correction, extraction and wavelength calibration, using standard slit spectroscopy routines in the Image Reduction and Analysis Facility (IRAF) suite.³

We show in Fig. 3 both NIR K_s -band spectra obtained in 2011 January and March, where we clearly see two strong lines in emission: He I and Br γ . We show in Fig. 4 a zoom on the region including the Br γ line, to see the evolution of its profile between the two observing dates. We also report in Table 1 the characteristics of He I and Br γ lines: wavelength, equivalent width (EW) and FWHM. We estimate the uncertainty of these parameters to ~ 10 per cent due to

³ IRAF is distributed by the National Optical Astronomy Observatory, which is operated by the Association of Universities for Research in Astronomy (AURA) under cooperative agreement with the National Science Foundation. IRAF is available online at <http://iraf.noao.edu/>

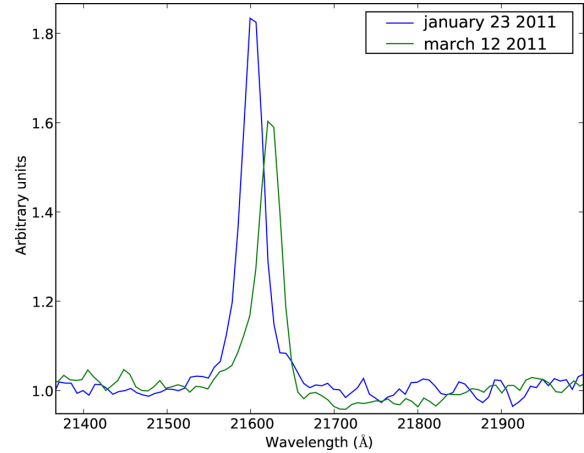


Figure 4. ESO/VLT NIR K_s -band spectra obtained on 2011 January 23 and March 12, enlarged on the region including the Br γ line.

Table 1. Identified lines in ESO/VLT NIR K_s -band spectra obtained on 2011 January 23 and March 12.

Date	Line	λ_{lab} (Å)	λ_{fit} (Å)	EW (Å)	FWHM (Å)
January	He I	20580	20531	−10.6	35.3
March	He I	20580	20549	−10.1	32.2
January	Br γ	21661	21601	−25.2	30.3
March	Br γ	21661	21622	−20.4	32.0

spectra analysis and localization of the continuum by eye inspection (using the IRAF task *splot*). The overall uncertainty on wavelength calibration is due both to the instrumental resolution and to extraction of lamp spectrum, which are of the order of ~ 0.3 and ~ 2 nm respectively. Some lines appear at fit wavelength offset with respect to their laboratory position, with an offset greater in January than in March (see Table 1). While this offset might be created by Doppler effect of ejecta outflowing from the decretion disc, since we do not detect any similar offset at optical wavelengths, we cannot exclude the possibility that this offset is due to larger uncertainty on wavelength calibration.

By comparing these NIR K_s -band spectra to the optical spectrum exhibiting a strong H α line, and to the series of optical spectra centred on the He I 6678 line, we observe the same general tendency both in optical and infrared, i.e. in both cases the EW of H α and Br γ lines gradually decrease between 2011 January and March [cf. Fig. 1 panel e with Fig. 4 and Table 2 with Table 1]. In addition, the Br γ line is asymmetric (as the He I 6678 line), with the blue wing slightly wider in March than in January, which is reminiscent of the asymmetric double peaked He I 6678 line. This asymmetry may indicate either the presence of a spiral density wave in the disc as suggested by the observations of He I 6678 line, or even a truncation of the disc size between the compact object and the companion star (such as described in Okazaki & Negueruela 2001; Okazaki et al. 2011). We note that the asymmetric wing could also be explained by the presence of ejecta outflowing from the decretion disc.

Finally, we notice that, while the intensity of the He I line remains stable, the one of the Br γ line decreases between January and March observations, which might indicate a change in ionization in the part of the disc where these lines are created.

Table 2. Journal of 2010–2011 optical spectroscopic observations of PSR B1259–63 and properties of the Be circumstellar disc of LS 2883 (see Section 8.1 for details).

Date	MJD (d)	$t - t_p$ (d)	$W_{H\alpha}$ (Å)	W_{6678} (Å)	r (R_*)	ρ_0 ($10^{-11} \text{ g cm}^{-3}$)	R_{disc}/R_*	M_{disc} ($10^{-8} M_{\odot}$)
2010-12-05	555 35.362	−9	−62.3	−0.44	33.6	2.82	8.8	1.31
2010-12-09	555 39.341	−5	−62.0	−0.39	28.1	2.79	9.1	1.16
2010-12-12	555 41.997	−3	−64.5	−0.39	25.7	3.03	9.5	1.19
2010-12-15	555 45.304	1	−66.4	−0.46	24.9	3.20	9.7	1.24
2010-12-18	555 48.312	4	−70.0	−0.52	26.4	3.56	10.0	1.43
2010-12-20	555 49.997	5	−73.0	−0.48	28.1	3.86	10.2	1.61
2010-12-23	555 53.305	9	−74.8	−0.55	32.5	4.05	10.1	1.85
2010-12-24	555 54.342	10	−74.4	−0.52	34.0	4.00	10.0	1.88
2011-01-01	555 62.319	18	−74.7	−0.56	47.4	4.04	9.3	2.31
2011-01-29	555 90.226	46	−61.6	−0.40	91.2	0.60	7.7	0.50
2011-02-04	555 96.000	52	−59.7	−0.45	99.2	0.58	7.5	0.51
2011-02-12	556 04.290	60	−58.0	−0.43	110.0	0.44	7.4	0.39
2011-02-14	556 06.307	62	−57.2	−0.42	112.6	0.44	7.3	0.38
2011-03-07	556 27.231	83	−56.6	−0.35	137.3	0.43	7.3	0.38
2011-03-08	556 28.002	83	−56.3	−0.37	138.2	0.43	7.3	0.38
2011-03-15	556 35.002	90	−57.2	−0.43	145.7	0.44	7.3	0.38
2011-03-19	556 39.002	94	−57.2	−0.42	149.9	0.44	7.3	0.38
2011-03-23	556 43.163	98	−56.2	−0.42	154.2	0.43	7.2	0.38
2011-04-03	556 54.003	109	−55.4	−0.42	164.9	0.42	7.2	0.37
2011-04-06	556 57.003	112	−54.0	−0.38	167.8	0.42	7.1	0.37
2011-05-17	556 98.004	153	−54.6	−0.31	203.3	0.42	7.1	0.37

4 OPTICAL SPECTROSCOPY

Spectroscopic observations of LS 2883, the optical counterpart of PSR B1259–63, were performed with the CTIO 1.5 m telescope, operated by SMARTS consortium,⁴ between UT dates 2010 December 5 and 2011 May 17. We used the RC spectrograph in service observing mode with the standard SMARTS grating setup 47/1b (grating 47 in 1st order) with the GG495 order sorting filter to achieve a wavelength coverage of 5630–6940 Å and a resolving power $R = \lambda/\Delta\lambda = 2500$ in the vicinity of the H α line. We observed LS 2883 for 3×300 s each night for a total of 21 nights. Neon comparison lamp spectra were obtained before and after the sequence for wavelength calibration. The spectra were zero corrected, flat fielded, extracted and wavelength calibrated using standard slit spectroscopy routines in IRAF. For each night of observations, we co-added the available spectra to improve the signal-to-noise ratio (S/N) of weak lines, especially He I $\lambda 6678$, before rectifying the mean spectrum to a unit continuum using line-free regions. The mean spectrum is shown in Fig. 5.

Over the six months of our observations, we detected changes in the overall strength of the H α emission but no significant line profile variations. The EW of the H α line, $W_{H\alpha}$, was measured by integrating over the emission line profile. We use the convention that an emission line has a negative $W_{H\alpha}$, so the absolute value of $W_{H\alpha}$ is shown in Fig. 1, panel e. Although the He I $\lambda 6678$ line has much lower S/N than H α , we also measured its EW, W_{6678} . The errors in $W_{H\alpha}$ and W_{6678} are about 5 and 10 per cent, respectively, due to noise and continuum placement. We compare W_{6678} (multiplied by 100 for better contrast) and $W_{H\alpha}$ in panel e of Fig. 1. Although there is more scatter in the W_{6678} measurements, we found that the overall strength of He I $\lambda 6678$ generally tracks the strength of H α well. Table 2 lists the UT date, MJD, time relative to periastron passage, measured $W_{H\alpha}$ and measured W_{6678} values for each observation in columns 1–5.

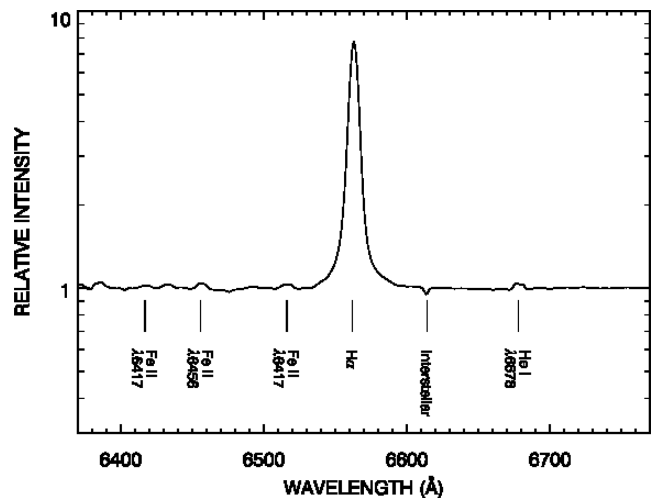


Figure 5. The mean H α spectrum of LS 2883 is plotted with several other faint emission lines. The relative intensity is plotted on a log scale to emphasize the weaker emission lines.

A growth of the EW of the H α line was observed from $-W_{H\alpha} \simeq 62$ Å around 5 d before periastron until $-W_{H\alpha} \simeq 75$ Å about 10 d after it. A decrease in $W_{H\alpha}$ was observed later, although the poor sampling only allows us to constrain the start of the decrease between $t_p + 18$ and $t_p + 46$ d, when it was back to $-W_{H\alpha} = 62$ Å (note that a baseline level of $-W_{H\alpha} = 54$ Å was measured at apastron by Negueruela et al. 2011). We interpret the observed behaviour as the growth/decay of the mass and size of the Be star disc, caused by the interactions with the pulsar/pulsar wind. Unfortunately due to data sparsity we do not know the exact date when the behaviour of the line EW starts to decrease, but if future observations during following periastron passages confirm the possible coincidence of the decrease of $W_{H\alpha}$ with the onset of the gamma-ray flare, then it could point to a possible triggering mechanism of the flare: an

⁴ <http://www.astro.yale.edu/smarts>

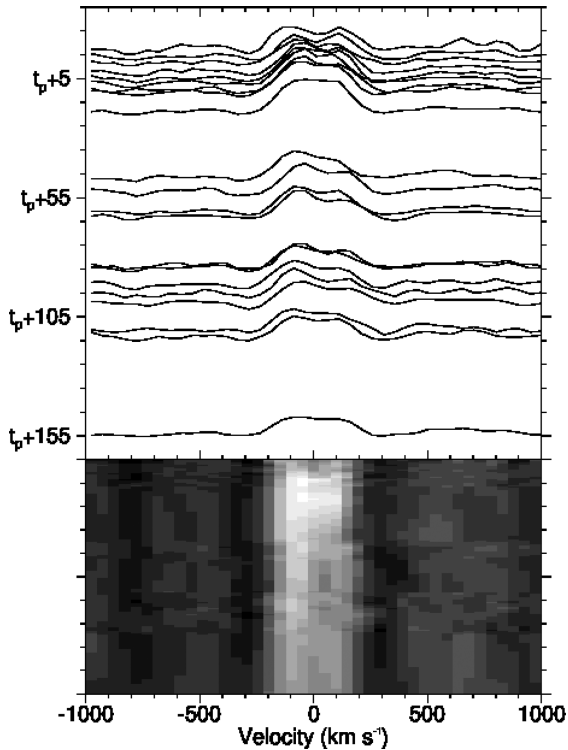


Figure 6. The upper plot shows the He I $\lambda 6678$ line profile of LS 2883 over the six months of observation, sorted by MJD, and the lower plot shows a grey-scale image of the same line. The intensity at each velocity in the grey-scale image is assigned one of 16 grey levels based on its value between the minimum (dark) and maximum (bright) observed values. The intensity between observed spectra is calculated by a linear interpolation between the closest observed phases.

abrupt change in the state of the circumstellar disc of the massive star. We explore this possibility in more detail in the Section 8.1.

Fig. 6 shows the evolution of the He I $\lambda 6678$ line profile. Despite the low resolving power of our observations, in most of our spectra the line is resolved with a clear double-peaked shape. The profile is symmetric within the limits of the S/N during the initial period up to $\sim t_p + 20$ d. At later times, the line shows a clear excess in the blue side (negative velocities) of the line relative to the red.

5 X-RAY OBSERVATIONS AND RESULTS

We conducted an X-ray monitoring campaign on PSR B1259–63 with *XMM–Newton* *Swift* and *Suzaku* telescopes, covering the period between $t_p - 131$ and $t_p + 79$ d. These observations are summarized in Tables 3–5. Each of these tables lists an identifier for the data set, UT date, MJD, time relative to periastron passage, true anomaly of the orbit and exposure time for each observation.

5.1 *XMM–Newton* observations

The log of the *XMM–Newton* data analysed in this paper is presented in Table 3. In all *XMM–Newton* observations, the source was observed with the European Photon Imaging Cameras MOS1, MOS2 (den Herder et al. 2001) and PN (Strüder et al. 2001) detectors in the small window mode with a medium filter. The *XMM–Newton* Observation Data Files were obtained from the online Science Archive⁵ and analysed with the Science Analysis Software (SAS) v11.0.0. Dur-

ing the data cleaning, all events that have energies above 10 keV and a count rate higher than 0.5 cts s^{-1} for the PN or 0.35 cts s^{-1} for the MOS detectors were removed.

The event lists for spectral analysis were extracted from a 22.5 arcsec radius circle for the MOS1 and MOS2 observations and from a 45 arcsec radius circle for the PN observations. For the spectral analysis, we made a simultaneous fit to the MOS1, MOS2 and PN data without imposing constraints on the intercalibration factors. The values of the MOS1 and MOS2 intercalibration factors f_{mos1} , f_{mos2} relative to the PN are given in the last two columns of Table 3.

5.2 *Swift* observations

Swift has closely monitored the PSR B1259–63 2010 periastron passage, and the data log is shown in Table 4. The *Swift*/X-ray Telescope (Gehrels et al. 2004) data were taken in photon mode with 500×500 window size. We processed all the data with standard procedures using the `FTOOLS`⁶ task `xrtpipeline` (version 0.12.6 under the `HEASOFT` package 6.12). We extracted source events from a circular region with a radius of 1 arcmin, and to account for the background we extracted events from a nearby circle of the same radius. Due to the low count rate (less than 0.4 cts s^{-1}), no pile up correction was necessary.

After spectral extraction, the data were rebinned with a minimum of 25 counts per energy bin to allow χ^2 fitting. The ancillary response file was generated with `xrtmkarf`, taking into account vignetting and point spread function (PSF) corrections. In our analysis we used the `swxpc0t012s6_20070901v011.rmf` spectral redistribution matrix for observations Sw5, Sw10, Sw11 and Sw12. For Sw6, Sw7, Sw8, Sw9 `swxpc0t012s6_20010101v013.rmf` was used instead.

The first set of *Swift* observations was taken in 2010 August, when the source flux was rather weak. After checking that the spectrum of the source varies only within the error limits during these observations, we combined all the *Swift* August data in order to have better statistics (Sw5 observation).

5.3 *Suzaku* observations

There were three *Suzaku* observations taken shortly after the 2010 periastron passage of PSR B1259–63 (see Table 5). The *Suzaku* observations were performed with three X-ray CCDs (the X-ray Imaging Spectrometers or XISs; Koyama et al. 2007) in the range 0.3–12 keV and the Hard X-ray Detector (HXD; Takahashi et al. 2007) in the range 13–600 keV. The XISs consists of one back-illuminated CCD camera (XIS-1) and two front-illuminated CCDs (XIS-0 and XIS-3). In this paper we discuss only the results of the XIS observations, while the HXD data will be discussed in a separate paper. Our analysis was performed using the `HEASOFT` software package (version 6.12).

We analysed the XIS data using pipeline processing version 2.5.16.29. We made use of cleaned event files of the XIS observations, with standard event screening applied. The standard screening procedures include event grade selections and the removal of time periods such as the spacecraft passage through the South Atlantic Anomaly, intervals of small geomagnetic cutoff rigidity, and times of low elevation angle. We found that XIS-0 gives somewhat lower N_{H} than others, which is most likely caused by imperfect calibrations due to the recently changed behaviour of contamination

⁵ http://xmm.vilspa.esa.es/external/xmm_data_acc/xsa/index.shtml

⁶ <http://heasarc.gsfc.nasa.gov/docs/software>

Table 3. Journal of 2011 *XMM–Newton* observations of PSR B1259–63.

Data set	Date	MJD (d)	$t - t_p$ (d)	ϕ (°)	Exposure (ks)	f_{mos1}	f_{mos2}
X14	2011-01-06	555 67.7	22	86.14	13.49	1.020 ± 0.007	0.967 ± 0.007
X15	2011-02-02	555 94.8	49	112.26	13.58	1.05 ± 0.01	1.05 ± 0.01
X16	2011-03-04	556 24.2	79	278.57	8.10	1.02 ± 0.02	1.05 ± 0.02

Table 4. Journal of 2010–2011 *Swift* observations of PSR B1259–63.

Data set	Date	MJD (d)	$t - t_p$ (d)	ϕ (°)	Exposure (ks)
Sw5	2010-08-06	554 14.3	–131	210.6	2.98
	2010-08-08	554 16.0	–129	210.8	3.29
	2010-08-09	554 17.4	–128	211.1	3.34
	2010-08-12	554 20.0	–125	211.5	2.41
	2010-08-15	554 23.2	–122	212.0	3.19
Sw6	2010-11-20	555 20.2	–25	255.2	3.87
Sw7	2010-11-25	555 25.6	–19	264.5	4.18
Sw8	2010-11-30	555 30.5	–14	276.5	3.36
Sw9	2010-12-14	555 44.6	–1	355.6	4.30
Sw10	2011-01-19	555 80.7	35	117.0	3.98
Sw11	2011-01-20	555 81.0	36	117.2	4.17
Sw12	2011-01-22	555 83.7	38	119.5	4.13

Table 5. Journal of 2011 *Suzaku* observations of PSR B1259–63.

Data set	Date	MJD (d)	$t - t_p$ (d)	ϕ (°)	Exposure (ks)
Sz9	2011-01-05	555 66.8	22	99.6	90.0
Sz10	2011-01-24	555 85.6	41	121.0	40.3
Sz11	2011-02-02	555 94.2	49	126.5	21.5

buildup. Thus we report the results from XIS-1 and XIS-3 only. A joint spectral fitting of XIS-1 and XIS-3 was done in the energy range of 0.4–9.5 keV.

5.4 The X-ray light curve

Panel c of Fig. 1 shows the X-ray light curve of the system. Observations made with different instruments at close orbital phases are consistent with each other, demonstrating good intercalibration.

From data obtained at orbital phases similar to the archival observations of previous periastron passages, one can see that the system orbital light curve is stable over several year time-scales. The stability of the orbital light curve allows us to use old and new data simultaneously while analysing the orbital evolution of the flux. The sharp rise of the X-ray flux at $t \sim t_p - 25$, probably related to the pulsar entering the Be star disc, in 2010 was closely followed by *Swift* (observations Sw6–Sw8). During this time, the flux increased by a factor of 4 in 9 d (note that due to the sparse observations, we probably missed the maximum flux). As the pulsar moved towards the periastron passage, the flux gradually decreased, reaching a local minimum that is only half the peak value near the periastron. Afterwards, we followed the system through its second passage near the disc, when we again observed an increase in flux to a value approximately 1.4 times higher than the maximum value observed during the first disc crossing. After that, the X-ray flux gradually decreased in a good agreement with previous observations, showing no unusual behaviour during the time of the GeV flare.

5.5 Spectral analysis

The X-ray spectral analyses were done with NASA/GSFC *XSPEC* v12.7.1 software package. A simple power law with a photoelectric absorption describes the data well, with no evidence for any line features. In Table 6 we present the results of the three parameter fits to the *XMM–Newton*, *Swift* and *Suzaku* data in the 0.5–10 keV energy range. The uncertainties are given at the 1σ statistical level and do not include systematic uncertainties. The quality of the *Swift* data does not allow us to look for both spectral slope and absorption column density, so we decided to fix the latter to the value $N_{\text{H}} = 5 \times 10^{21} \text{ cm}^{-2}$ consistent with the value found in the *XMM–Newton* and *Suzaku* observations.

Similar to the observations of previous periastron passages, we found that several months before the periastron the spectral index was quite soft, $\Gamma \sim 1.8$. It became much harder a month before periastron, as the flux started to increase. The spectrum softened a bit as the flux reached its maximum, but it remained harder than $\Gamma = 1.5$. The spectrum softened again as the pulsar approached periastron and entered the disc for the second time. At the moment when the X-ray luminosity reached its second peak the slope was softer than $\Gamma = 1.7$. As the X-ray luminosity started to decrease the slope remained close to 1.5, except during the very last *XMM–Newton* observation, when the slope became hard again, reaching the value $\Gamma = 0.42$ previously observed at $t - t_p = +266$ d (Chernyakova et al. 2006).

6 FERMI-LAT OBSERVATIONS AND RESULTS

The *Fermi Gamma-ray Space Telescope* was launched on 2008 June 11, from Cape Canaveral, Florida. The LAT is an electron–positron pair production telescope, featuring solid state silicon trackers and cesium iodide calorimeters, sensitive to photons from ~ 20 MeV to greater than 300 GeV (Atwood et al. 2009). Relative to earlier γ -ray missions, the LAT has a large ~ 2.4 sr field of view, a large effective area ($\sim 8000 \text{ cm}^2$ for >1 GeV on axis) and improved angular resolution (PSF is better than 1° for 68 per cent containment at 1 GeV). The *Fermi* survey mode operations began on 2008 August 4. In this mode, the observatory is rocked north and south on alternate orbits to provide more uniform coverage so that every part of the sky is observed for about 30 min every 3 h.

The analysis of the *Fermi*-LAT data in this paper is similar to the method used in Abdo et al. (2011b). We used the P7SOURCE data set and the associated P7SOURCE_V6 instrument response functions. The analysis was performed using the *Fermi* SCIENCE TOOLS 09-27-01 package.⁷ A zenith angle cut of $<100^\circ$ was applied to the data to reject atmospheric γ -rays from the Earth’s limb. The standard binned maximum likelihood analysis was performed on events extracted from a $20^\circ \times 20^\circ$ region around the location of PSR B1259–63 in the energy range 0.1–300 GeV. The source

⁷ FSSC is available online at <http://fermi.gsfc.nasa.gov/ssc/data/analysis/software/>

Table 6. Spectral parameters for 2010–2011 observations of PSR B1259–63.

Data set	$t - t_p$ (d)	$F(1-10 \text{ keV})$ ($10^{-11} \text{ erg cm}^{-2} \text{ s}^{-1}$)	Γ	N_H (10^{22} cm^{-2})	$\chi^2(\text{ndof})$
Sw5	−127	$0.17^{+0.01}_{-0.02}$	1.8 ± 0.09	0.5	8.3 (14)
Sw6	−25	$0.69^{+0.08}_{-0.16}$	$0.99^{+0.13}_{-0.23}$	0.5	3.6 (7)
Sw7	−19	1.53 ± 0.12	1.33 ± 0.08	0.5	25.48 (24)
Sw8	−14	$2.60^{+0.12}_{-0.16}$	1.37 ± 0.06	0.5	61.73 (35)
Sw9	−1	$1.72^{+0.11}_{-0.08}$	1.56 ± 0.05	0.5	47.9 (39)
Sz9	22	3.56 ± 0.01	1.76 ± 0.01	0.56 ± 0.01	2177 (2454)
X14	22	$3.25^{+0.01}_{-0.02}$	1.71 ± 0.01	0.48 ± 0.04	2220 (2029)
Sw10	35	$2.31^{+0.08}_{-0.11}$	1.51 ± 0.06	0.5	36.1 (41)
Sw11	36	$2.19^{+0.09}_{-0.10}$	1.48 ± 0.06	0.5	44.7 (42)
Sw12	38	$2.02^{+0.12}_{-0.05}$	1.44 ± 0.06	0.5	33.2 (41)
Sz10	41	2.08 ± 0.02	1.53 ± 0.01	0.51 ± 0.01	1566 (1528)
X15	49	$1.61^{+0.02}_{-0.01}$	1.45 ± 0.01	0.44 ± 0.01	1418 (1453)
Sz11	49	$1.77^{+0.02}_{-0.04}$	1.46 ± 0.02	0.48 ± 0.01	749 (769)
X16	79	$1.13^{+0.02}_{-0.01}$	1.37 ± 0.02	0.42 ± 0.01	855(851)

model used in the maximum likelihood analysis included 2 yr (2FGL) *Fermi* catalogue (Nolan et al. 2012) γ -ray sources within the analysed region, PSR B1259–63 and the diffuse Galactic and extragalactic components. Galactic diffuse emission was modelled using the `gal_2yearp7v6_v0.fits` model, and the isotropic diffuse component was modelled using the `iso_p7v6source.txt` model. The LAT data analysed in this paper covers the 4.5 yr period between 2008 August 4 and 2013 February 19. This covers the time period over which the pulsar was near apastron until well after the passage of the pulsar through the dense equatorial disc of the Be star.

First we analysed the whole 4.5 yr of available data, modelling the spectrum of each point source with a catalogue model. The normalizations and indexes of catalogue point sources as well as the normalization of the extragalactic diffuse background were then fixed to their best-fitting values in order to build the PSR B1259–63 light curve around the periastron. The power-law index of PSR B1259–63 was fixed to the best-fitting value (2.86) obtained for the time period around the periastron passage. Afterwards, the normalizations of PSR B1259–63, Galactic diffuse background and the sources marked as variable in 2FGL catalogue (within 5° from PSR B1259–63) were left free, similar to the procedure used by Abdo et al. (2011b).

Panel b in Fig. 1 shows the LAT flux light curve. All data points have a significance higher than 2σ . The upper limits on the figure correspond to 95 per cent confidence limit. The time binning was selected to be 7 d for the period of the flare and 14 d otherwise. The light curve shows upper limits until $t_p - 25$ d, detections around a flux level of $0.5 \times 10^{-6} \text{ cm}^{-2} \text{ s}^{-1}$ between $t_p - 25$ and $t_p + 16$ d, and the GeV flare that reaches a flux level of $2 \times 10^{-6} \text{ cm}^{-2} \text{ s}^{-1}$ at $t_p + 30$ and decays in a roughly linear way, with the last detection at a flux level of $0.5 \times 10^{-6} \text{ cm}^{-2} \text{ s}^{-1}$ between $t_p + 65$ and $t_p + 80$ d. The results obtained in this paper are consistent with those in the earlier work by Abdo et al. (2011b).

7 HESS OBSERVATIONS AND RESULTS

The High Energy Stereoscopic System (HESS) is an array of imaging atmospheric Cherenkov telescopes located in the Khomas Highland of Namibia at an altitude of 1800 m above sea level. HESS phase I (consisting of four 13 m diameter telescopes) is optimized

for the detection of very high-energy gamma-rays in the range of 100 GeV to 20 TeV. The total field of view is 5° and the angular resolution of the system is $\lesssim 0.1$. The average energy resolution is about 15 per cent. The HESS I array is capable of detecting point sources with a flux of 1 per cent of the Crab nebula flux at a significance level of 5σ in 25 h when observing at low zenith angles (Aharonian et al. 2006).

Observations of PSR B1259–63 around its 2010 periastron passage resulted in a rather small data set compared to observations around the 2004 (Aharonian et al. 2005) and 2007 (Aharonian et al. 2009) periastron passages. The collected data correspond to a live time of about 6 h (HESS Collaboration 2013). Observations were performed over five nights, 2011 January 9/10, 10/11, 13/14, 14/15 and 15/16, which corresponds to the period from $t_p + 26$ to $t_p + 32$ with respect to the time of periastron.

The source was detected at the 11.5σ level (Li & Ma 1983) at a position compatible with previous HESS observations. The differential spectrum of the source follows a simple power law with a flux normalization at 1 TeV $N_0 = (1.95 \pm 0.32_{\text{stat}} \pm 0.39_{\text{syst}}) \times 10^{-12} \text{ TeV}^{-1} \text{ cm}^{-2} \text{ s}^{-1}$ and spectral index $\Gamma = 2.92 \pm 0.30_{\text{stat}} \pm 0.20_{\text{syst}}$. The integral flux above 1 TeV averaged over the entire observation period is $F(E > 1 \text{ TeV}) = (1.01 \pm 0.18_{\text{stat}} \pm 0.20_{\text{syst}}) \times 10^{-12} \text{ cm}^{-2} \text{ s}^{-1}$ (HESS Collaboration 2013). The nightly light curve over the observation period (panel a in Fig. 1) is compatible with a constant flux and does not show any hint of source variability (HESS Collaboration 2013).

Both the flux level and spectral shape from 2011 are in a very good agreement with results obtained for previous periastron passages. Moreover, the comparison of results obtained in 2011 and 2004 observations, which were taken at similar orbital phases, provides a stronger evidence of the repetitive behaviour of PSR B1259–63 (see Fig. 1; HESS Collaboration 2013). Such comparison was not possible using the 2004 and 2007 data sets as observations were performed at different phases before and after periastron.

HESS observations provide a three-day overlap ($t_p + 30$; $t_p + 32$) in time with the GeV flare detected by *Fermi*. This allows the direct study of a possible flux enhancement in the TeV band over the time-scale of the GeV flare. A careful statistical study showed no evidence of any significant flux enhancement, which leads to the conclusion that the GeV flare emission is of a different nature than the TeV emission (HESS Collaboration 2013).

8 DISCUSSION

The broad-band non-thermal emission from the PSR B1259–63 system is produced in the interaction of the relativistic pulsar wind with the stellar wind of the massive Be star. The high eccentricity of the orbit is responsible for the episodic nature of the source activity, with bright outbursts occurring during the periods of the pulsar’s close passage near the massive star. The characteristic ‘double peak’ structure of the orbital light curves of the source in the radio, X-ray and, possibly, TeV gamma-ray bands is naturally interpreted as occurring due to the inhomogeneity of the stellar outflow of the fast-rotating Be star. The peaks of the non-thermal emission are associated with the periods of the pulsar’s passage through the denser and slower gas in the equatorial disc of the Be star. This behaviour has also been observed during the previous periastron passages and is clearly seen in the radio and X-ray bands also during the 2010–2011 periastron passage, shown in Fig. 1.

The orbit-to-orbit light curves in the radio band, which are qualitatively similar with the maxima occurring at similar orbital phases, exhibit up to ~ 50 per cent differences in the overall flux level between different periastron passages (Johnston et al. 2005). Contrary to the radio light curve, the behaviour of the source in the X-ray band is remarkably stable. Measurements of the X-ray flux at the same orbital phases, spaced by several 3.4 yr orbital periods, reveal nearly the same flux.

Fermi LAT observations of the 0.1–10 GeV gamma-ray activity of the source during the 2010–2011 periastron passage have revealed a puzzling flaring activity, which occurred after the periastron passage and also after the post-periastron transit of the equatorial disc of the Be star by the pulsar. The GeV flaring activity was remarkable in the sense that the energy output of the source in this band reached a theoretical maximum given by the spin-down luminosity of the pulsar, 8×10^{35} erg s $^{-1}$, assuming isotropic emission in this energy band. Abdo et al. (2011b) have noticed that the GeV band flare was peculiar in the sense that it had no obvious counterparts at lower energies, in the radio and X-ray bands.

The broad-band observations of the source reported here generally support the conclusion of Abdo et al. (2011b) on the ‘orphan’ nature of the GeV flare. The only data that could reveal an irregularity in the source behaviour coincident in time with the moment of the GeV flare are the optical spectroscopic data shown in panel e of Fig. 1. These data show a clear decrease of the EW of the H α line that could coincide with the GeV flare. A gap in the optical spectroscopy data during the period 18–46 d after the periastron does not allow us to tell if the decrease of $W_{\text{H}\alpha}$ is exactly coincident with the moment of the GeV flare (30 d after the periastron). However, it seems that the decrease of the line strength is delayed with respect to the start of the radio outburst that happened 15 d after the periastron. The peculiar behaviour of the H α line and its possible relation to the GeV flare deserve special attention.

8.1 Evolution of the Be star disc mass and size based on the H α line measurements

With multiple observations of $W_{\text{H}\alpha}$ available, we can estimate the changing size and mass of the circumstellar disc through the periastron passage. Grundstrom & Gies (2006) describe a simple model to measure the ratio of the projected effective disc radius (the radius at which half of the H α emission originates) to the stellar radius, R_{disc}/R_* , and the density at the base of the disc, ρ_0 , using $W_{\text{H}\alpha}$, the stellar effective temperature T_{eff} , and disc inclination angle i_{disc} as input parameters.

Negueruela et al. (2011) found that LS 2883 is highly distorted due to its rapid rotation, with a polar radius (or equivalent non-rotating radius) $R_* = 8.1 R_\odot$ and a bulging equatorial radius $R_{*,\text{eq}} = 9.7 R_\odot$. The equator is significantly cooler than the poles (27 500 versus 34 000 K) due to gravity darkening. They also found that the Be star is inclined with 33° and has an angular velocity Ω of about 88 per cent of the critical rotation value at which the centrifugal force at the equator equals the gravitational force. Using a Roche model for such a rapidly rotating star (Maeder 2009), we find that the mean temperature averaged over the stellar surface is about 30 200 K, so we define T_{eff} accordingly.

For LS 2883, the Be disc should be highly truncated near periastron, both due to the gravitational influence of the pulsar (which is observed in other Be binaries using long baseline optical interferometry; Gies et al. 2007) and due to disruption by the pulsar wind ram pressure (predicted by simulations of Okazaki et al. 2011; Takata et al. 2012). The truncation distance expands rapidly after periastron passage. Therefore we used the orbital solution of Wang et al. (2004), a stellar mass of $31 M_\odot$ (Negueruela et al. 2011), and the typical neutron star mass of $1.4 M_\odot$ to calculate the binary separation distance, r , as a function of time. The separation values range from $24.8R_* < r < 203.3R_*$ over the course of our observations. We fixed the outer disc boundary to r when the stars are close ($r < 100R_*$), and we used an outer boundary of $100R_*$ in accordance with the recommendation of Grundstrom & Gies (2006) for times when $r > 100R_*$.

To estimate the total mass of the disc, we used an axisymmetric, isothermal density distribution,

$$\rho(r, z) = \rho_0 \left(\frac{R_*}{r} \right)^n \exp \left[-\frac{1}{2} \left(\frac{z}{H(r)} \right)^2 \right] \quad (1)$$

(Carciofi & Bjorkman 2006) and a radial density exponent $n = 3$, typical of other Be star discs (Gies et al. 2007). The scaleheight of the disc is

$$H(r) = H_0 \left(\frac{r}{R_*} \right)^\beta, \quad (2)$$

where

$$H_0 = \frac{a}{V_{\text{crit}}} R_*, \quad (3)$$

$$a = \sqrt{\frac{kT}{\mu m_{\text{H}}}} \quad (4)$$

and $\beta = 1.5$ for an isothermal disc (Bjorkman & Carciofi 2005; Carciofi & Bjorkman 2006). We integrated this density distribution from the equatorial stellar surface at $R_{*,\text{eq}}$ out to the disc truncation radius, described above, to estimate the total disc mass, M_{disc} .

The resulting ρ_0 , R_{disc}/R_* and M_{disc} are listed in Table 2. We emphasize that these disc measurements should be viewed with caution since our assumption of an axisymmetric, isothermal disc is overly simplistic. Deviations from this simple disc structure may produce order of magnitude variations in the calculated mass, and these effects are discussed more thoroughly by McSwain et al. (2008). A further source in error for our disc mass measurement is the truncation radius assumed in our model. For a pulsar orbit that is inclined 90° relative to the Be disc, the separation distance when the pulsar becomes eclipsed by the disc, $42.2R_*$, is slightly higher than the periastron distance. This implies slightly higher disc masses near periastron. However, if the disc is truncated instead at the star’s effective Roche lobe radius, then we predict slightly lower

disc masses. These revised masses are well within the order of magnitude error that is inherent to the assumptions of our model.

Within our model we found that the Be disc grew in mass as the binary went through periastron passage in 2010 December. Tidal disruption by the neutron star may have triggered this sudden growth in disc mass. Moreno, Koenigsberger & Harrington (2011) find that the rate of energy dissipation over the stellar surface reaches a maximum amplitude near or slightly after periastron passage in very eccentric binaries, prompting an increase in stellar activity near that orbital phase. Other Be stars (e.g. δ Sco; Miroshnichenko et al. 2001, 2003) have been observed to exhibit disc outbursts around the time of periastron passage, so the disc growth of LS 2883 is not unusual.

The times of GeV flaring in PSR B1259–63 correspond to an epoch of disc reduction. We speculate that the GeV flaring could be due to the interaction of a mass stream being pulled away from the disc to collide with the relativistic pulsar’s wind.

Additional information on the properties of the disrupted disc could be found from the He I $\lambda 6678$ line profile, shown in Fig. 6. Despite the low resolving power of our observations, in most of our spectra the line is resolved with a clear double-peaked shape. During the disc growth period, the peaks are symmetric within the limits of the S/N. However, during the disc reduction period, the He I $\lambda 6678$ line shows a clear excess on the blue side of the line (negative velocities) relative to the red one. The asymmetry is sustained for at least ~ 60 d, far longer than the expected 1–2 d required for disc material to circle the star. The asymmetry may indicate a slowly moving spiral density wave in the disc, typical of density waves observed in other Be stars (Porter & Rivinius 2003). The pulsar wind probably does not significantly alter the ionization levels in the circumstellar disc. Since He I will ionize at a lower temperature than H I, it would be expected to be fully ionized near periastron if the pulsar wind’s influence on the disc produces strong ionization effects. However, we observe that the H α and He I $\lambda 6678$ line strengths track each other well in Fig. 1, and no significant deviations are found within the limits of noise. The similarities with other Be stars in binary systems, which suffer gravitational disruption, and the non-alteration of the disc ionization, suggest that the disc disruption seen in the optical data might simply be driven by gravitational tidal forces instead of a pulsar interaction.

8.2 The radio outflow during the GeV flare

The high-energy particle outflow from the system is unresolved in most of the energy bands except for the radio. Both previously reported high-resolution observations in the radio band (Moldón et al. 2011) and the observations reported here reveal the extended nature of the radio source, about 50 mas in size. At a distance $d \simeq 2$ kpc (Negueruela et al. 2011), this corresponds to a projected linear size of the source $R \simeq 1.5 \times 10^{15} [d/2 \text{ kpc}] \text{ cm}$, which is two orders of magnitude larger than the orbital separation at periastron. Our analysis of the high-resolution LBA image obtained 29 d after the 2010 periastron passage has two important implications.

First, we have found a radio structure that is very similar to the one found 21 d after the 2007 periastron passage (see fig. 1 middle in Moldón et al. 2011). This confirms the presence of an extended structure in each periastron passage and their similar appearances, albeit with a slightly more negative PA in the image presented here. This may be a consequence of the different orbital phases of the observations, and it will be discussed in a future paper including four additional LBA observations conducted around the 2010 periastron passage.

Secondly, the position of the pulsar is determined for the first time with the same data used to obtain the radio morphology of the nebula extending towards the north-west, allowing us to make a direct measurement of the pulsar’s position inside the nebula. We found that the pulsar is located around 5 mas towards south-east of the peak of the radio nebula. This is still marginally compatible with the predicted pulsar position in the 2007 periastron passage (see the red cross in fig. 1 middle in Moldón et al. 2011), which was an indirect estimation affected by unmodelled ionospheric uncertainties that also depended on the uncertain proper motion of the binary system and on the orbital motion of the pulsar around the massive star. With the relative positions of the pulsar and the nebula obtained here, we find that the overall morphology of the source is consistent with a cometary tail extending behind the pulsar.

The projected displacement of the peak of the nebular emission from the pulsar position, $R_r \simeq 1.5 \times 10^{14} [d/2 \text{ kpc}] \text{ cm}$, provides an estimate of the distance scale at which the optical depth becomes comparable to the free-free absorption, which suppresses the radio emission from the innermost region. The measured distance to the radio emitting region is in a good agreement with the estimate of Zdziarski, Neronov & Chernyakova (2010)

$$R_r \simeq 2 \times 10^{14} \left[\frac{\dot{M}_w}{10^{-7} M_\odot \text{ yr}^{-1}} \right]^{2/3} \left[\frac{v_\infty}{10^8 \text{ cm s}^{-1}} \right]^{-2/3} \times \left[\frac{\nu}{2.3 \text{ GHz}} \right]^{-2/3} \left[\frac{T}{3 \times 10^4 \text{ K}} \right]^{-1/2} \left[\frac{f}{0.1} \right]^{-1/3} \text{ cm} \quad (5)$$

for a typical mass-loss rate of the Be star \dot{M}_w , asymptotic speed, v_∞ , clumping factor, f , and temperature, T , of the stellar wind. For PSR B1259–63 the terminal velocity of the wind was estimated to be $1350 \pm 200 \text{ km s}^{-1}$ (McCullum 1993).

The radio emission is produced via the synchrotron mechanism by electrons with energies (Zdziarski et al. 2010)

$$E_{e,r} \simeq 0.1 \left[\frac{B_r}{10 \text{ mG}} \right]^{-1/2} \left[\frac{\nu}{1 \text{ GHz}} \right]^{1/2} \text{ GeV}, \quad (6)$$

where B_r is the strength of magnetic field in the radio emission region. If such electrons are (a) injected during the GeV flare and (b) are able to escape towards the radio emission region with the speed comparable to the speed of light, they would reach the radio emission region in less than two hours from the start of the flare. Therefore, the absence of a radio counterpart of the GeV flare (mostly from archival data at similar orbital phases) implies that either the 100 MeV electrons are not injected during the flare or they escape at a speed much lower than the speed of light.

Slow escape of the radio-emitting plasma has been recently revealed in the observations of another gamma-ray loud binary system, LS I +61 303 (Chernyakova et al. 2012), in which the speed of the high-energy particle loaded outflow was found to be comparable to the speed of the stellar wind. Adopting such a model for the PSR B1259–63 system would imply a time delay $t_r = R_r/v_\infty \simeq 17$ d for the radio ‘echo’ of the GeV flare. This time period was not covered by the ATCA radio observations reported here [see panel d of Fig. 1], so it remains unclear whether the GeV flare was associated with a delayed radio counterpart or whether electrons with energies in the ~ 0.1 GeV range were injected in the flare. No evidence of such a flare is present in the archival data [see panel d of Fig. 1 for the details of 2004 periastron passage], but at the moment we do not know whether the GeV flare occurs each periastron passage so we cannot make any firm conclusions.

8.3 X-ray and TeV observations

Similarly to the radio observations, neither X-ray nor the TeV observations reveal obvious counterparts to the GeV flare. However, contrary to the radio emission, the X-ray and TeV emission are, most probably, produced directly inside the binary orbit so that no time delay of the X-ray and TeV band emission is expected.

Although the time coverage of the HESS TeV light curve during the 2010–2011 periastron passage is not sufficient to draw definitive conclusions on the presence/absence of the TeV flaring activity during the whole period of the GeV band flare, a careful statistical study showed no evidence of any significant flux enhancement in TeV energy band right at the beginning of the GeV flare (HESS Collaboration 2013). Moreover, one could notice from the top panel of Fig. 1 that the TeV flux measurements one month after the periastron are consistent with the previous measurements during the 2004 periastron passage at similar times. This indicates that the orbit-to-orbit behaviour of the source in the TeV band might be stable, similar to the behaviour in the X-ray band. In fact, the X-ray and TeV band flux might be produced by one and the same electron population with \sim TeV energies, via the synchrotron and inverse Compton (IC) mechanisms. If this is the case, one could combine the 2004 and 2010–2011 data into an orbit-folded light curve. Such a light curve would reveal a broad post-periastron maximum compatible with the post-periastron maxima of the X-ray and radio light curves, but there is no pronounced maximum occurring at the moment of the GeV band flare (see Fig. 1).

In the X-ray band, non-simultaneous data from different periastron passages are compatible with the interpretation that the post-periastron maximum of the light curve may have a two-peak structure (see Fig. 1). Based on the observed trend in the post-periastron X-ray light curve, we should expect the X-ray flux about 30 d after the periastron to decline. However, instead we see that the 2007 *Chandra* flux at $t_p + 29$ d is comparable to the 2010 measurements by *Suzaku* and *XMM–Newton* some 22 d after the periastron. Thus, the flux observed by *Chandra* in 2007 at $t_p + 29$ d might be an X-ray counterpart to a GeV flare (if the GeV flare is a periodic phenomenon). However, similarly to the case of the TeV observations, it is not possible to draw definitive conclusions on the presence/absence of the X-ray counterpart of the GeV flare because of the lack of the systematic monitoring of the source close to the flare period.

Repeated observations of the source during the next periastron passage, with a denser time coverage both in X-rays and in the TeV band, are essential to clarify the existence of the X-ray and TeV counterparts of the GeV flare as well as the question of the recurrent nature of the flare.

8.4 Possible connection of the Be star disc perturbation and the GeV flare

In this paper we discuss the possibility that the detected GeV flare could be related to the reduction in the size/mass of the equatorial disc of the massive Be star in the system. Unfortunately, a gap in the $H\alpha$ data does not allow us to make a firm identification of the start of the GeV flare with the start of the decrease of the EW of the $H\alpha$ line. The possibility of triggering the flare by the disc disruption event has to be verified with the future observations with denser coverage of the $H\alpha$ measurements around the onset of the flare.

The decrease of $W_{H\alpha}$ and the enhanced blue wing of the $He\text{I } \lambda 6678$ line indicate the presence of strong perturbations in the interacting pulsar wind–stellar wind system. In the absence of per-

turbation of the Be star disc, the relativistic particles can escape from the system along a bow-shaped contact surface of the pulsar and stellar winds and in a direction opposite to the contact surface apex. A part of the pulsar wind power emitted not in the direction of the bow shock apex is able to escape to large distances, like in a typical large-scale pulsar wind nebula. Only the power emitted in the direction of the bow shock is converted to radiation.

In the model discussed in Kong, Cheng & Huang (2012) the observed X-ray and GeV emission is explained as synchrotron emission from the post-shock relativistic electrons Doppler boosted at the particular orbital phase. This model is able to describe the observed spectra pretty well, but fails to explain the substantial shift of the X-ray and GeV light curve peaks.

In the modelling one should take into account that the strong perturbation of the disc destroys the regular bow-shaped contact surface between the pulsar and stellar outflow. It is possible that the fly-by of the disc material near the pulsar destroys the regular geometry of the relativistic particle and electromagnetic field flow in the unshocked pulsar wind. Once the magnetic field in the pulsar wind ceases to be aligned with the particle flow, high-energy particles in the wind immediately lose their energy via synchrotron radiation. In such a scenario the energy of electrons responsible for the GeV flare should be in the 100 TeV range:

$$E_{e,\text{flare}} \simeq 10^2 \left[\frac{B_{\text{pw}}}{1 \text{ G}} \right]^{-1/2} \left[\frac{v}{1 \text{ GHz}} \right]^{1/2} \text{ TeV} \quad (7)$$

assuming that magnetic field in the pulsar wind is at the level of $B_{\text{pw}} \sim 1$ G at distances comparable to the binary separation distance ($\sim 10^{13}$ cm). The energy of electrons responsible for the highest energy synchrotron emission is in the 100 TeV range, which is close to the PeV energies of electrons responsible for the recently discovered GeV flares of the Crab pulsar/pulsar wind nebula system (Abdo et al. 2011a; Buehler et al. 2012). This suggests a possibility that, in both sources, the flares could be produced via the same mechanism. In the case of the Crab flares, the short time-scale $t_{\text{crab}} < 1$ d of the variability suggests a relatively compact size of the flaring source of $l_{\text{crab}} \leq 10^2$ au. This distance scale is comparable to the size of the extended source revealed by the VLBI observations of PSR B1259–63. Taking this into account, the appearance of 100 TeV electrons responsible for the γ -ray synchrotron emission in the PSR B1259–63 system does not appear unreasonable.

In the synchrotron scenario, the duration of the flare is estimated by the time of the fly-by of the disc material near the pulsar, so that 10–30 d is a reasonable estimate, assuming a typical speed of the stellar wind and taking the binary separation distance as the estimate of the size of the region occupied by the pulsar wind.

The absence of the flare counterparts in the radio, X-ray and TeV bands could also be reasonably explained by the high efficiency of synchrotron energy losses for the 100 TeV particles. Most of the power of the pulsar wind is converted into the GeV band emission, with only minor fraction of the power left for emission at much lower energies. Synchrotron cooling of the 100 TeV particles would form a characteristic $dN/dE \sim E^{-2}$ low-energy tail in the electron distribution. The spectrum of synchrotron emission from this low-energy tail would have a slope $dN_\gamma/dE \sim E^{-1.5}$, so that the power emitted in the X-ray band is some ~ 3 orders of magnitude lower than the power of the GeV band emission. Taking into account that the luminosity of IC emission in the TeV band is comparable to the luminosity of the X-ray emission, one arrives at a conclusion that no TeV band counterpart of the flare is expected to be detectable.

An alternative possibility is that the GeV flaring emission is produced via the IC, rather than synchrotron, mechanism. Such a

possibility was considered by Khangulyan et al. (2012). In this case, the energies of electrons in the unshocked pulsar wind are much lower, in the GeV range. A fraction of the observed GeV emission from the system is thus produced via IC scattering of the UV radiation coming either directly from the Be star or from its circumstellar disc by the unshocked pulsar wind electrons. The fraction of the GeV flux produced in this way depends on the geometry of the region occupied by the unshocked pulsar wind. The luminosity of the IC emission from the unshocked pulsar wind could strongly increase if the volume occupied by the unshocked pulsar wind increases. This scenario requires a very high efficiency of re-processing stellar radiation in the Be star disc, with up to a half of the UV luminosity of the system being due to the emission from the disc, rather than from the star.

A strong perturbation of the equatorial disc of the Be star could, in principle, lead to an enhancement of the luminosity of the IC emission from the unshocked pulsar wind. Indeed, a natural consequence of the destruction of the disc is that the volume occupied by the unshocked pulsar wind rapidly grows. Electrons/positrons in the unshocked pulsar wind propagate to larger distances and could give away a larger fraction of their energy to the IC radiation while remaining in the unshocked wind. With a suitable assumption about the UV luminosity of the circumstellar disc (which turns out to be very high, exceeding the stellar luminosity, possibly as a result of local heating of the Be star disc by the pulsar crossing, see Khangulyan et al. 2012), one could find that nearly 100 per cent of the spin-down luminosity of the pulsar could be converted into gamma-ray power in the unshocked wind if its volume becomes sufficiently large during the flare.

A potential problem of such a scenario would be to explain why the IC luminosity of the system does not reach the spin-down luminosity of the pulsar before the destruction of the disc. Indeed, before the disc destruction, the volume occupied by the unshocked pulsar wind is small so that the efficiency of the IC energy loss in the unshocked pulsar wind zone is low. As a result, the IC luminosity of the unshocked wind is much less than 100 per cent of the spin-down power. However, electrons and positrons from the pulsar wind do not stop to lose energy via the IC emission when they enter the shocked pulsar wind zone at the same rate as in the unshocked pulsar wind zone. If the unshocked pulsar wind electrons/positrons release 100 per cent of their energy into the IC emission while escaping from the system during the flaring period, the shocked pulsar wind electrons/positrons should also release 100 per cent of their energy via the same channel while escaping through the shocked pulsar wind before the flare. Thus, the IC luminosity of the system is expected to be at 100 per cent of the pulsar spin-down power throughout the pulsar's passage through the disc, not only at the moment of the disc destruction. A possible way out of this difficulty might be the existence of an alternative non-radiative channel of energy dissipation of the pulsar wind electrons/positrons in the shocked pulsar wind region, a question that requires further investigation.

Besides the optical photons coming from the star and the disc, X-ray photons produced by the shocked pulsar wind can act as seed photons for the observed GeV emission. Such a possibility was discussed by Pétri & Dubus (2011) and Dubus & Cerutti (2013). In Pétri & Dubus (2011) GeV emission is generated rather close to the pulsar, and the X-ray photons are scattered by the relativistic pairs in the striped pulsar wind. In this case the GeV flare was interpreted by the authors as a lucky combination of the geometry and the presence of additional seed photons coming from the shocked region. In the Dubus & Cerutti (2013) model the GeV emission is due to the IC

scattering of the X-ray photons by the shocked relativistic wind. In this model the GeV flare is expected to peak near the inferior conjunction, but the reason of the delay between the X-ray and GeV peak in this model is not clear.

Mochol & Kirk (2013) interpret the observed flare as IC scattering of the optical photons on the precursor of superluminal waves roughly 30 d after the periastron passage. This model does not require an additional source of photons, but it is unclear what triggers the formation of the precursor well after the exit from the disc. This model also predicts a pre-periastron flare, which has not been observed at any wavelength.

9 CONCLUSIONS

In this paper, we have reported the results of multiwavelength observations of PSR B1259–63 during its 2010 periastron passage. This was the first periastron for which complete monitoring in the high-energy gamma-ray band was available. These data have revealed a puzzling GeV flare occurring $\simeq 30$ d after the periastron (Abdo et al. 2011b). Our multiwavelength data show that the source behaviour in the radio and X-ray band is qualitatively similar to the previous periastron passages and that there are no obvious counterparts of the GeV flare in other wavebands, from radio to TeV gamma-rays. However, both in the X-rays and radio data from previous periastron passages there might be small irregularities in the behaviour of the light curves at the moment of the onset of the GeV flare. The possible relation of these irregularities to the GeV flare has to be verified with simultaneous data during future multiwavelength campaign for the next periastron passage.

The orbital light curves in the radio band do exhibit orbit-to-orbit variations. On the other hand, the X-ray light curve is remarkably stable. This might be related to the fact that the X-ray emission is produced directly inside the binary system, while the radio emission is produced by the high-energy outflow reaching distances 10–100 times larger than the binary system size. The time coverage of the source in the TeV band is not sufficient to judge whether the source is variable from orbit to orbit.

Optical spectroscopy data reveal the evolution of the H α line strength, which indicates changes in the state of the circumstellar disc of the Be star induced by the close passage of the pulsar. The pulsar first induces growth of the disc in mass and size. The disc growth stops after the periastron passage and further interaction of the pulsar/pulsar wind with the disc leads to a perturbation of the disc structure, which possibly triggers the GeV band flare. This perturbation manifests itself in the reduction of the EWs of the H α and He I $\lambda 6678$ lines. On the other hand, the disc disruption that we observe may be a normal occurrence in binary Be systems due to gravitational interactions near the close passage. Unfortunately, the optical spectroscopy data have a gap at the moment of the onset of the GeV flare, so we are not able to make an unambiguous link between the flare onset and changes in the Be star disc state. This possible link should be verified with a denser optical spectroscopy coverage of the periastron passage in 2014.

We have measured for the first time the position of the pulsar and the unpulsed extended emission from the same data set in the radio band. Such a measurement removes the systematic uncertainty related to the cross-calibration of different data sets which has affected previous measurements. This measurement pinpoints the position of the binary system within an extended radio emission region of the size ~ 100 au. We find that the overall morphology of the radio source is compatible with a ‘cometary tail’ extending behind the pulsar.

There are a number of open questions that should be addressed in new multiwavelength observations during the next periastron passage in 2014. In particular, it is not clear whether the GeV flare is recurrent and, if it is, whether it occurs at a particular orbital phase. The triggering mechanism of the flare has to be clarified. We should investigate more deeply possible multiwavelength signatures of the triggering mechanism of the flare with new simultaneous observations densely covering the time span of the flare. Our results point to a possible relationship between the GeV flare and changes in the Be star disc state. These changes could hopefully be traced by the variations of the strength of emission lines from the disc or of its column density.

ACKNOWLEDGEMENTS

The *Fermi* LAT Collaboration acknowledges support from a number of agencies and institutes for both development and the operation of the LAT as well as scientific data analysis. These include NASA and DOE in USA, CEA/Irfu and IN2P3/CNRS in France, ASI and INFN in Italy, MEXT, KEK and JAXA in Japan, and the K. A. Wallenberg Foundation, the Swedish Research Council and the National Space Board in Sweden. Additional support from INAF in Italy and CNES in France for science analysis during the operations phase is also gratefully acknowledged.

The Parkes radio telescope and the Australian LBA are part of the Australia Telescope which is funded by the Commonwealth Government for operation as a National Facility managed by CSIRO. We thank our colleagues for their assistance with the radio timing observations. This work made use of the Swinburne University of Technology software correlator, developed as part of the Australian Major National Research Facilities Programme and operated under licence.

AN is grateful to the Swiss National Science Foundation for the support under grant PP00P2_123426/1. MVM is grateful for support from the National Science Foundation under grant AST-1109247 and from NASA under DPR number NNX11AO41G. JM, MR and JMP acknowledge support by the Spanish Ministerio de Economía y Competitividad (MINECO) under grants AYA2010-21782-C03-01 and FPA2010-22056-C06-02. JM acknowledges support by MINECO under grant BES-2008-004564. MR acknowledges financial support from MINECO and European Social Funds through a *Ramón y Cajal* fellowship. JMP acknowledges financial support from ICREA Academia.

Based on observations made with ESO Telescopes at the La Silla Paranal Observatory under programme ID 086.D-0511. This work was supported by the Centre National d'Etudes Spatiales (CNES), based on observations obtained with MINE – the Multiwavelength INTEGRAL Network.

The authors thank the International Space Science Institute (ISSI, Bern) for support within the ISSI team ‘Study of Gamma-ray Loud Binary Systems’ and SFI/HEA Irish Centre for High-End Computing (ICHEC) for the provision of computational facilities and support.

REFERENCES

Abdo A. A. et al., 2011a, *Science*, 331, 739
 Abdo A. A. et al., 2011b, *ApJ*, 736, L11
 Aharonian F. et al., 2005, *A&A*, 442, 1
 Aharonian F. et al., 2006, *A&A*, 457, 899
 Aharonian F. et al., 2009, *A&A*, 507, 389
 Atwood W. B. et al., 2009, *ApJ*, 697, 1071

Bjorkman J. E., Carciofi A. C., 2005, in Ignace R., Gayley K. G., eds, *ASP Conf. Ser. Vol. 337, Modeling the Structure of Hot Star Disks*. Astron. Soc. Pac., San Francisco, p. 75
 Buehler R. et al., 2012, *ApJ*, 749, 26
 Carciofi A. C., Bjorkman J. E., 2006, *ApJ*, 639, 1081
 Chernyakova M., Neronov A., Lutovinov A., Rodriguez J., Johnston S., 2006, *MNRAS*, 367, 1201
 Chernyakova M., Neronov A., Aharonian F., Uchiyama Y., Takahashi T., 2009, *MNRAS*, 397, 2123
 Chernyakova M., Neronov A., Molokov S., Malyshev D., Lutovinov A., Pooley G., 2012, *ApJ*, 747, L29
 den Herder J. W. et al., 2001, *A&A*, 365, L7
 Dubus G., Cerutti B., 2013, *A&A*, 557, A127
 Gehrels N. et al., 2004, *ApJ*, 611, 1005
 Gies D. R. et al., 2007, *ApJ*, 654, 527
 Grundstrom E. D., Gies D. R., 2006, *ApJ*, 651, L53
 HESS Collaboration, 2013, *A&A*, 551, A94
 Hirayama M., Cominsky L. R., Kaspi V. M., Nagase F., Tavani M., Kawai N., Grove J. E., 1999, *ApJ*, 521, 718
 Johnston S., Manchester R. N., Lyne A. G., Bailes M., Kaspi V. M., Qiao G., D’Amico N., 1992, *ApJ*, 387, L37
 Johnston S., Manchester R. N., Lyne A. G., D’Amico N., Bailes M., Gaensler B. M., Nicastro L., 1996, *MNRAS*, 279, 1026
 Johnston S., Manchester R. N., McConnell D., Campbell-Wilson D., 1999, *MNRAS*, 302, 277
 Johnston S., Ball L., Wang N., Manchester R. N., 2005, *MNRAS*, 358, 1069
 Khangulyan D., Aharonian F. A., Bogovalov S. V., Ribó M., 2012, *ApJ*, 752, L17
 Kirk J. G., Ball L., Skjaeraasen O., 1999, *Astropart. Phys.*, 10, 31
 Kong S. W., Cheng K. S., Huang Y. F., 2012, *ApJ*, 753, 127
 Koyama K. et al., 2007, *PASJ*, 59, 23
 Li T.-P., Ma Y.-Q., 1983, *ApJ*, 272, 317
 McCollum B., 1993, *BAAS*, 25, 1321
 McSwain M. V., Huang W., Gies D. R., Grundstrom E. D., Townsend R. H. D., 2008, *ApJ*, 672, 590
 Maeder A., 2009, *Astronomy and Astrophysics Library, Physics, Formation and Evolution of Rotating Stars*. Springer, Berlin, doi:10.1007/978-3-540-76949-1
 Melatos A., Johnston S., Melrose D. B., 1995, *MNRAS*, 275, 381
 Miroshnichenko A. S. et al., 2001, *A&A*, 377, 485
 Miroshnichenko A. S. et al., 2003, *A&A*, 408, 305
 Mochol I., Kirk J. G., 2013, *ApJ*, 776, 40
 Moldón J., Johnston S., Ribó M., Paredes J. M., Deller A. T., 2011, *ApJ*, 732, L10
 Moldón J., Ribó M., Paredes J. M., 2012, *A&A*, 548, A103
 Moreno E., Koenigsberger G., Harrington D. M., 2011, *A&A*, 528, A48
 Negueruela I., Ribó M., Herrero A., Lorenzo J., Khangulyan D., Aharonian F. A., 2011, *ApJ*, 732, L11
 Nolan P. L. et al., 2012, *VizieR Online Data Catalog*, 219, 90031
 Okazaki A. T., Negueruela I., 2001, *A&A*, 377, 161
 Okazaki A. T., Nagataki S., Naito T., Kawachi A., Hayasaki K., Owoccki S. P., Takata J., 2011, *PASJ*, 63, 893
 Pavlov G. G., Chang C., Kargaltsev O., 2011, *ApJ*, 730, 2
 Pétri J., Dubus G., 2011, *MNRAS*, 417, 532
 Porter J. M., Rivinius T., 2003, *PASP*, 115, 1153
 Smith D. A. et al., 2008, *A&A*, 492, 923
 Strüder L. et al., 2001, *A&A*, 365, L18
 Takahashi T. et al., 2007, *PASJ*, 59, 35
 Takata J. et al., 2012, *ApJ*, 750, 70
 Tam P. H. T., Huang R. H. H., Takata J., Hui C. Y., Kong A. K. H., Cheng K. S., 2011, *ApJ*, 736, L10
 Tavani M. et al., 1996, *A&AS*, 120, 221
 Wang N., Johnston S., Manchester R. N., 2004, *MNRAS*, 351, 599
 Weltevrede P. et al., 2010, *Publ. Astron. Soc. Aust.*, 27, 64
 Zdziarski A. A., Neronov A., Chernyakova M., 2010, *MNRAS*, 403, 1873

This paper has been typeset from a $\text{\TeX}/\text{\LaTeX}$ file prepared by the author.